

RECONSTRUCTION OF RESPIRATORY-BINNED CARDIAC SPECT USING A ROBUST SMOOTHING PRIOR

Chao Song, Yongyi Yang, Miles N. Wernick, P. Hendrik Pretorius¹, and Michael A. King¹

Department of Electrical and Computer Engineering, Illinois Institute of Technology, Chicago, IL 60616, USA

¹Department of Radiology, University of Massachusetts Medical School, Worcester, MA 01655, USA

ABSTRACT

Cardiac images in single photon emission computed tomography (SPECT) are known to suffer from loss of resolution associated with respiratory motion. In this work, we investigate the use of a spatially adaptive smoothing prior in a motion-compensated reconstruction framework for SPECT, wherein respiratory binned data are incorporated into the reconstruction of the myocardium with respect to a reference respiratory bin. In the experiments, we evaluated this approach with both simulated imaging data and two sets of clinical acquisitions. The results show that the proposed approach can be effective for improving the heart wall in terms of both the noise level and spatial resolution. The proposed approach was also demonstrated to be robust when the imaging dose was reduced.

Index Terms— Respiratory correction, cardiac SPECT, smoothing prior, non-local means.

1. INTRODUCTION

Single photon emission computed tomography (SPECT) can provide important diagnostic information about both myocardial perfusion and ventricular function, which is widely used for diagnosis of coronary artery disease [1]. However, the quality of SPECT images is also compromised by various factors including low data counts and motion blur (cardiac, respiratory, and even patient motion [2]), which inevitably could affect the diagnostic accuracy if not corrected for [3,4].

As in other modalities, e.g., CT, PET and MRI [5-7], respiratory binned (or gated) acquisition has been studied in SPECT for reducing the effect of respiratory motion, e.g., [8]. Respiratory binned acquisition can be achieved by monitoring either the temporal position in the respiratory cycle (called phase binning) or the magnitude of the respiratory motion (called amplitude binning) [9]. Due to the variability in respiratory patterns observed clinically, amplitude binning can be more accurate as it is directly correlated with the motion extent [9]. However, unlike in CT or PET, a unique challenge in SPECT is that the acquired data statistics could vary significantly among both projection angles and respiratory gate/binning intervals. If

not properly accounted for, such variations could lead to limited-angle artifacts [10].

Toward addressing this challenge, in our previous studies [10,11] we developed a compensating scheme for the uneven data statistics acquired at different projection angles, and demonstrated that it could effectively suppress the artifacts in reconstruction. We studied this scheme both in a post-reconstruction motion-correction approach [10] and in a joint statistical reconstruction approach [11]. In the first approach, the individual respiratory bins were reconstructed separately and combined with motion correction [10]; in the second approach, a reference bin was reconstructed from the acquired data of all respiratory bins through motion compensation [11]. The latter was demonstrated to yield more accurate results than the former.

In recent years, there have been growing interests in studying methods for reducing the dose in cardiac SPECT in order to minimize its associated radiation risk [12-15]. However, with reduced dose, the acquired data counts from a subject will be reduced accordingly. As a result, the issue of high imaging noise in SPECT is further exacerbated. This poses a challenge in image reconstruction, because increased smoothing is needed in order to suppress the elevated noise, which in turn will lead to additional loss in image resolution.

In this work we investigate the use of a spatially adaptive 3D smoothing prior in reconstruction of respiratory-binned SPECT images. In concept, this smoothing prior is derived from a 3D non-local means (NLM) filter, which we studied recently for post-processing of cardiac gated images [16]. In that study, an NLM filter was demonstrated to be rather effective for suppressing the noise in cardiac images while without adversely affecting the wall motion and resolution. Encouraged by this success, in this work we incorporate a 3D NLM smoothing prior into a respiratory-binned reconstruction scheme based on motion compensation [11]. As to be demonstrated in the experiments, this can lead to more robust results in the reconstruction when the imaging dose is significantly reduced (by as much as 50%).

We note that NLM based smoothing priors have been applied previously to achieve noise suppression and edge preservation in tomographic reconstruction applications [17-23]. For emission tomography, an NLM prior was used in

This work was supported by NIH/NHLBI Grant HL122484.

[24] for 3D cardiac SPECT reconstruction; in [25], an NLM prior was used for dynamic PET images. To our best knowledge, NLM priors have not been explored for reconstruction of respiratory binned/gated SPECT images.

2. METHODS

2.1 Respiratory-binned imaging model

In cardiac SPECT imaging, a rotating gamma camera is used to record the emitted photon events after a radiolabeled compound is introduced into the body. Due to the uneven nature of patient respiratory motion, the acquired data counts are no longer evenly distributed among both the projection angles and respiratory bins in respiratory-binned acquisition. To account for this variation, we incorporate a time factor for each projection angle and respiratory bin into the imaging model as in [10]. Specifically, assume that R respiratory bins and P projection angles are used. Let $\tau_{p,r}$ denote the actual acquisition time at angle p during respiratory bin r , and let \mathbf{h}_p denote the corresponding projection operator at angle p . Then the acquired data at angle p during respiratory bin r , denoted by vector $\mathbf{g}_{p,r}$, can be written as:

$$E[\mathbf{g}_{p,r}] = \tau_{p,r} \mathbf{h}_p \mathbf{f}_r + \mathbf{s}_{p,r}, r=1, \dots, R, p=1, \dots, P \quad (1)$$

where \mathbf{f}_r denotes the source distribution of bin r , $\mathbf{s}_{p,r}$ is the expected scatter component, and $E[\cdot]$ is the expectation operator characterizing the statistical nature of the data.

In (1), the operator \mathbf{h}_p denotes the system response sensitivity at angle p . In this study, both the collimator response and attenuation effect the incorporated into the system matrix. In addition, the timing information $\tau_{p,r}$ in (1) is obtained with list-mode acquisition.

2.2 Joint reconstruction with NLM smoothing

Given the acquired data in (1), our goal is to reconstruct the source distribution \mathbf{f}_r for a reference respiratory bin r_0 (ideally, without motion blur). To increase the signal-to-noise ratio in the reconstruction, we would like to make use of all the acquired data rather than bin r_0 alone. Conceptually, this can be accomplished by applying motion correction to each of the individual bins with respect to bin r_0 . A challenge, however, is that the motion information of the respiratory bins is not known *a priori* and needs to be determined from the imaging data. In this work, we estimated the image motion from a pre-reconstruction of the individual bins in (1) (Section 2.5).

For convenience, let $r_0=1$ denote the reference respiratory bin. We use this reference to describe the rest of the respiratory bins \mathbf{f}_r through a motion-compensation model. Specifically, we write \mathbf{f}_r as:

$$\mathbf{f}_r = \mathbf{M}_r \mathbf{f}_1, r=2, \dots, R \quad (2)$$

where \mathbf{M}_r is the motion-compensation operator between bin r and the reference.

With (2), the imaging data in the different bins in (1) can be rewritten with respect to the common reference as:

$$E[\mathbf{g}_{p,r}] = \tau_{p,r} \mathbf{h}_p \mathbf{M}_r \mathbf{f}_1 + \mathbf{s}_{p,r}, p=1, \dots, P \quad (3)$$

for $r=2, \dots, R$.

In this work, we seek a maximum *a posteriori* (MAP) solution for the reference image \mathbf{f}_1 . For convenience, let \mathbf{g}_r denote the collection of acquired data of bin r over all the camera angles, i.e., $\mathbf{g}_r \equiv [\mathbf{g}_{1,r}^T, \dots, \mathbf{g}_{P,r}^T]^T$. Due to the independence of the data statistics among the different bins, the log-likelihood of the data over all the respiratory bins can be written as:

$$L(\mathbf{f}_1) = \sum_{r=1}^R \log p(\mathbf{g}_r | \mathbf{f}_1, \mathbf{M}_r) \quad (4)$$

where $p(\mathbf{g}_r | \mathbf{f}_1, \mathbf{M}_r)$ denotes the likelihood term of bin r parameterized by the reference image \mathbf{f}_1 . Note that \mathbf{M}_1 is simply the identity operator. Poisson statistics is used for the imaging data in this study.

Then the MAP estimate for the unknown \mathbf{f}_1 is obtained as:

$$\hat{\mathbf{f}}_1 = \arg \max_{\mathbf{f}_1} [L(\mathbf{f}_1) + \log p(\mathbf{f}_1)] \quad (5)$$

where $p(\mathbf{f}_1)$ is a prior distribution on \mathbf{f}_1 .

Toward achieving adaptive spatial smoothing, we consider a Gibbs prior for $p(\mathbf{f}_1)$ in the following form:

$$p(\mathbf{f}_1) \propto \exp[-\beta U_{NLM}(\mathbf{f}_1)] \quad (6)$$

where $U_{NLM}(\mathbf{f}_1)$ is a potential function to be defined below, and β is a scalar parameter used to control the level of smoothing.

The potential function $U_{NLM}(\mathbf{f}_1)$ in (6) is given as follows:

$$U_{NLM} = \sum_{i=1}^N [\mathbf{f}_1(i) - \hat{\mathbf{f}}_1(i)]^2 \quad (7)$$

where $\hat{\mathbf{f}}_1(i)$ is the output at voxel i of a non-local means (NLM) filter applied to \mathbf{f}_1 . Specifically, $\hat{\mathbf{f}}_1(i)$ is given by:

$$\hat{\mathbf{f}}_1(i) = \frac{1}{Z} \sum_{j \in N^i} w(i, j) \mathbf{f}_1(j) \quad (8)$$

where the summation term is a weighted average of the voxels in the neighborhood N^i of voxel i within the reference bin, and Z is a normalization factor for the filter to have unity DC gain.

In (8), the weight factors $w(i, j)$ are used to measure the similarity level between voxels i and j based on a small image patch centered at their respective locations. Specifically, they are defined as:

$$w(i, j) = \exp \left\{ - \sum_m \left[\mathbf{f}_1(l_i^m) - \mathbf{f}_1(l_j^m) \right]^2 / h_s^2 \right\} \quad (9)$$

where l_i^m denotes voxel m within the patch centered at voxel i , and l_j^m denotes its corresponding voxel within the patch at voxel j . In addition, h_s is a kernel parameter used to control the bandwidth of spatial smoothing.

It is noted that the form of $\hat{\mathbf{f}}_1(i)$ in (8) is motivated by our recent work in [16], where the image value at voxel i is predicted from a weighted average of voxels from within the

same respiratory bin. The weight factors $w(i, j)$ are used to achieve adaptive smoothing based on the similarity level of the neighborhood voxels to voxel i .

Given that the image \mathbf{f}_1 is not known beforehand, in our experiments a pre-reconstruction of \mathbf{f}_1 was used for determining the weight factors in (9) (Section 2.5). In addition, based on the results in [16], a window size of $3 \times 3 \times 3$ was used for the neighborhood in (8), and a window size of $5 \times 5 \times 5$ was used for the image patch in the weight factors in (9). The kernel parameter was set as $h_s = 0.1$.

For optimization of (4), in our experiments we used the modified block sequential regularized expectation maximization (BSREM) algorithm, which is known to be globally convergent [26]. A total of 16 subsets were used in our implementation.

2.3 Evaluation study

In the experiments, we first evaluated the proposed reconstruction approach with simulated imaging data where the ground truth is known. Afterward, we demonstrated the reconstruction approach on two sets of clinical data. To demonstrate the robustness of the proposed approach, we evaluated the reconstruction not only at conventional imaging dose but also at a much reduced dose level.

To quantify the overall accuracy of the reconstructed myocardium, we compute the normalized mean squared error (NMSE) of a volumetric region containing the entire myocardium, which is defined as:

$$NMSE = \frac{\|\mathbf{f} - \hat{\mathbf{f}}\|_{ROI}^2}{\|\mathbf{f}\|_{ROI}^2} \quad (10)$$

where \mathbf{f} and $\hat{\mathbf{f}}$ denote the reference and reconstructed images, respectively, and ROI denotes the volumetric region (a 2D transversal slice of it is shown in Fig. 1).

As reference, the reconstruction from the noiseless projection of the source (without attenuation) is used. This represents the ideal case of reconstruction without any distortion in acquisition.

In addition, we also examine the spatial resolution of the reconstructed heart wall by plotting the intensity profile of a section across the left ventricle (LV) (as illustrated in Fig. 3).

2.4 Imaging datasets

2.4.1 Simulation data

The 4D NURBS-based cardiac-torso (NCAT) 2.0 phantom was used to simulate SPECT imaging with Tc-99m labeled sestamibi as the imaging agent. The simulation was based on a Philips Prism 3000 SPECT system with a low-energy high-resolution (LEHR) collimator. The projection data was 64×64 bins with a pixel size of 0.634 cm. For a circular camera rotation of 28.5 cm radius, 64 projection sets were collected. To better simulate the continuous nature of data acquisition, a set of 3D source images was first generated over 28 equally spaced intervals within the extent of

diaphragm motion with 2 cm in the super inferior direction and 1.2 cm in the anteroposterior direction. Afterward, the 28 projection sets were rebinned into seven respiratory intervals based on amplitude. Attenuation and detector response effects were all included in the simulation.

To simulate the realistic distribution of acquisition among both projection angles and respiratory intervals, the acquisition time was rescaled according to five real clinical acquisitions. Subsequently, Poisson noise was introduced for each acquisition at 8 million (typical of a clinical acquisition) and 4 million counts (half dose) to simulate different dose levels. For quantitative evaluation, 10 noise realizations were simulated for each clinical acquisition, resulting in a total of 50 noise realizations.

2.4.2 Clinical data

As a preliminary demonstration, we also tested the proposed approach on two sets of clinical data, which were acquired under IRB approval with informed content. The dataset was acquired in list-model by a Philips BrightView SPECT/CT system with 64 projections over 180 degrees and a 128×128 matrix. The pixel size was 0.467 cm. Photon events were recorded within a symmetric energy window centered on 140.5keV with a width of 15%. A scatter window was also acquired which was centered at 120keV with a 5% width. Sequential transmission imaging was used for the estimation of attenuation maps. The acquired data were binned into seven respiratory intervals based on a visual tracking system. For reconstruction, the TEW method was used for scatter correction. For half dose acquisition, the photon events in the list-mode data were down-sampled with sensitivity reduced by 50% in the imaging period [12].

2.5 Reconstruction methods for comparison

For comparison, in our experiments we considered the following reconstruction methods: 1) the proposed approach with NLM smoothing prior (denoted by NLM), 2) the model-based motion-compensated reconstruction approach in [11] (denoted by MMC), and 3) reconstruction without respiratory compensation (denoted by Ungated). In the experiments, the respiratory motion was estimated from a pre-reconstruction of individual gates as in [11]. In addition, the weight factors in (9) were estimated from a pre-reconstruction of the reference respiratory bin with the OSEM algorithm (16 subsets, 10 iterations).

3. RESULTS

In Fig. 2, we show the NMSE results of the reconstructed myocardium by the proposed approach at both full- and half-dose levels. Each curve was obtained by varying the smoothing parameter β in (6). The β values used were as follows: 1) full dose: 0, 0.00001, 0.00002, 0.00003, 0.00005, 0.00007, and 0.0001; 2) half dose: 0, 0.00003, 0.00007, 0.0001, 0.00015, 0.0002, and 0.0003. Note that larger values of β were used for half-dose in order to accommodate the

increased imaging noise. These results were obtained from an average of 50 noise realizations. For comparison, the NMSE results are shown in Fig. 2 also for the MMC approach. As can be seen, the proposed NLM achieved lower reconstruction error (hence improved accuracy in the myocardium) than MMC at each dose level. For example, at full dose, for NLM the best NMSE = 0.0626 ($\beta=0.00007$), compared to the best NMSE = 0.0718 ($\beta=0.00003$) for MMC.

In Fig. 3 we show the intensity profile for a segment of the LV wall reconstructed by different methods at half-dose level (averaged from 50 noise realizations). The parameter β was set according to the optimal NMSE result for each method. The NLM profile is noted to be closer to the Ideal reference than the MMC. The variance of the NLM curve is also smaller than that of MMC (hence, lower noise). This indicates that the LV resolution is improved in NLM.

In Fig. 4 we show a set of reconstructed NCAT images by the different methods (parameter β set at optimal NMSE) at both full- and half-dose levels. For comparison, the Ideal reference and reconstruction without respiratory correction (“Ungated”) are also shown. It is noted that the LV wall is more uniform in NLM than in MMC, and the LV wall is also less blurry in NLM (particularly in long-axis view).

Finally, in Figs. 5 and 6 we show the reconstruction results from the clinical acquisitions at full- and half-dose levels by the different methods: Ungated, MMC, and NLM. At both dose levels, the LV wall is noted to be more uniform and better defined in NLM than in the other methods. The NLM images at half dose are noted to be almost identical to that at full dose.

4. CONCLUSION

We investigated the use of a spatially adaptive smoothing prior based on NLM filtering in reconstruction of respiratory-binned SPECT images. We demonstrated this approach with both simulated imaging and two sets of clinical data. The results show that it could effectively suppress the imaging noise and improve the LV wall resolution at reduced imaging dose. In future work we plan to further evaluate the proposed approach with perfusion detection tasks.

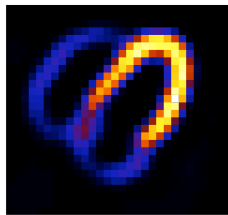


Fig. 1 A transversal slice of the myocardium.

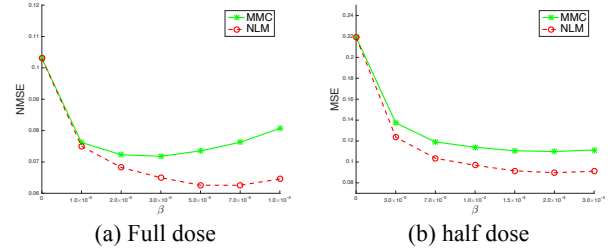


Fig. 2 NMSE of reconstructed myocardium at different dose levels.

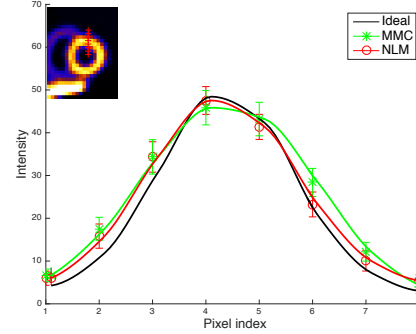


Fig. 3 Intensity profile of the reconstructed LV wall.

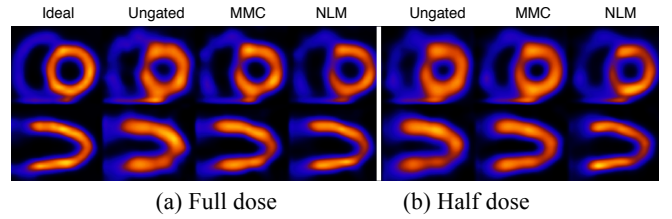


Fig. 4 Reconstruction of phantom acquisitions by different methods. 1st row: short-axis view; 2nd row: long-axis view.

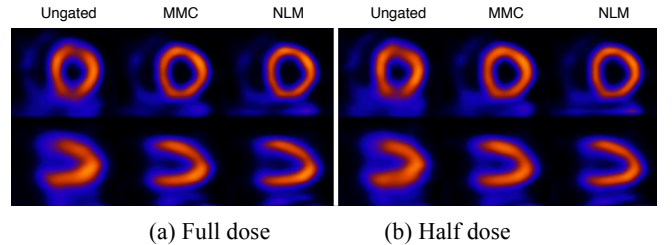


Fig. 5 Reconstruction of clinical acquisitions (patient#1).

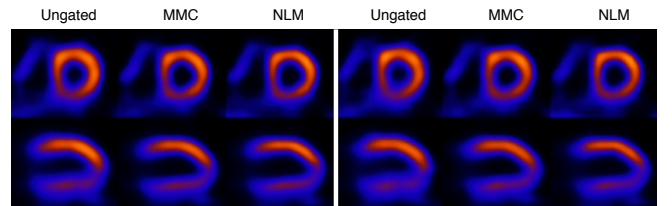


Fig. 6 Reconstruction of clinical acquisitions (patient#2).

5. REFERENCES

- [1] E.G. DePuey, and E.V. Garcia, "Updated Imaging guidelines for nuclear cardiology procedures part I," *J. Nucl. Cardiol.*, vol. 8, G5-G58, 2001.
- [2] J.A. Cooper, P.H. Neumann, *et al.*, "Effect of patient motion on tomographic myocardial perfusion imaging," *J. Nucl. Med.*, vol. 33, pp. 1566-1571, 1992.
- [3] W.P. Segars, and B.M.W. Tsui, "Study of the efficacy of respiratory gating in myocardial SPECT using the new 4D NCAT phantom," *IEEE Trans. Nucl. Sci.*, vol. 49, 2002.
- [4] X. Niu, Y. Yang, *et al.*, "Effects of motion attenuation and scatter corrections on gated cardiac SPECT reconstruction," *Med. Phys.*, vol. 32, pp. 6571-6585, 2011.
- [5] I.G. Buliev, C.T. Badea, *et al.*, "Estimation of the heart respiratory motion with applications for cone beam computed tomography imaging...", *IEEE Trans. Inf. Tech.* vol.7, 2003.
- [6] A.L. Kesner, R.A. Bundschuh, *et al.*, "Respiratory gated PET derived from raw PET data," *IEEE Nucl. Sci. Symp. Conf. Rec.*, vol. 4, pp. 2686-2691, 2007.
- [7] T. Nopopen, T. Kokki, *et al.*, "Spirometry based respiratory gating method for cardiac PET and MRI imaging," *IEEE Nucl. Sci. Symp. Conf. Rec.*, vol. 4, pp. 4832-4834, 2008.
- [8] K. Murase, M. Ishine, *et al.*, "Simulation and experimental study of respiratory motion effect on image quality of single phone emission computed tomography," *Eur J Nucl Med.*, vol. 13, pp. 244-249, 1987.
- [9] W. Lu, P. J. Parikh, *et al.*, "A comparison between amplitude and sorting and phase angle sorting use external respiratory measurement for 4D CT," *Med. Phys.*, vol. 33, 2006.
- [10] W. Qi, Y. Yang, M. N. Wernick, P. H. Pretorius, and M. A. King, "Reconstruction with angular compensation in respiratory-gated cardiac SPECT," *IEEE Inter. Conf. on Image Processing*, 2014.
- [11] W. Qi, Y. Yang, *et al.*, "Compensation of acquisition variations in respiratory-gated SPECT with joint statistical reconstruction," *IEEE Inter. Symp. Biomed. Imag.*, 2015.
- [12] M. Jin, X. Niu, *et al.*, "4D reconstruction for low-dose cardiac gated SPECT," *Med. Phys. Biol.*, vol. 40, 2013.
- [13] S. Agarwal, J. Dey, "Low-dose or better resolution ultrafast cardiac SPECT: NCAT reconstruction and GATE study," *IEEE Nucl. Sci. Symp. Conf. Rec.*, vol. 4, 2011.
- [14] E. G. DePuey, S. Bommireddipalli, *et al.*, "Wide beam reconstruction "quarter-time" gated myocardial perfusion SPECT functional imaging...", *J Nucl. Cardiol*, vol. 16, 2009.
- [15] N. Zafrir, A. Solodky, *et al.*, "Feasibility of myocardial perfusion imaging with half the radiation dose...", *J Nucl. Cardiol*, vol. 19, pp. 704-712, 2012.
- [16] C. Song, Y. Yang, *et al.*, "4D non-local means post-filtering for cardiac gated SPECT," *IEEE Inter. Imag. Proc. Conf.*, pp. 1200-1204, 2015.
- [17] Z. Bian, J. Huang, *et al.* "Iterative image reconstruction for low-dose x-ray CT using a sinogram restoration induced edge-preserving prior," *IEEE Inter. Symp. Biomed. Imag.*, 2014.
- [18] J. Wang, T. Li, *et al.* "Iterative image reconstruction for CBCT using edge-preserving prior," *Med. Phys.* vol. 36, 2009.
- [19] A. Raj, G. Singh, *et al.* "Bayesian parallel imaging with edge-preserving priors," *Magn. Reson. Med.* vol. 57, 2007.
- [20] C. Bouman, K. Sauer, "A generalized Gaussian image model for edge-preserving MAP estimation," *IEEE Trans. Imag. Proc.*, vol. 2, pp. 296-310, 1993.
- [21] M. Lassas, S. Siltanen, "Can one use total variation prior for edge-preserving Bayesian inversion," *Inverse Problem*, vol. 20, pp. 1537-1563, 2004.
- [22] I. Hsiao, A. Rangarajan, *et al.* "A new convex edge-preserving median prior with applications to tomography," *IEEE Trans. Imag. Proc.*, vol. 25, pp. 580-585, 2003.
- [23] M. Belge, M.E. Kilmer, *et al.* "Wavelet domain image restoration with adaptive edge-preserving regularization," *IEEE Trans. Imag. Proc.*, vol. 9, pp. 597-608, 2000.
- [24] D. Kazantsev, A. Bousse, *et al.* "Edge preserving bowsher prior with nonlocal weighting for 3D SPECT reconstruction," *IEEE Inter. Symp. Biomed. Imag.*, pp. 1158-1161, 2011.
- [25] Z. Bian, J. Ma, *et al.* "Dynamic PET image reconstruction using a spatial-temporal edge-preserving prior," *Nucl. Sci. Symp. Med. Imag. Conf.*, M17-12, 2013.
- [26] S. Ahn, J. A. Fessler, "Globally convergent image reconstruction for emission tomography using relaxed ordered subsets algorithms," *IEEE Trans on Med. Imag.*, vol. 22, pp. 613-626, 2003.